Title

Novel cryo-tomography workflow reveals nanometer-scale responses of epithelial cells to matrix stiffness and dimensionality

Journal

Molecular Biology of the Cell, 33(14)

ISSN

1059-1524

Authors

Gaietta, Guido
Kai, Fuiboon
Swift, Mark F
et al.

Publication Date

2022-12-01

DOI

10.1091/mbc.e22-03-0092

Peer reviewed

Novel cryo-tomography workflow reveals nanometer-scale responses of epithelial cells to matrix stiffness and dimensionality

Guido Gaietta[a,*], Fuiboon Kai[b], Mark F. Swift[a], Valerie M. Weaver[b], Niels Volkmann[a,c,*], and Dorit Hanein[a,d,*,†]

[a]Scintillon Institute, San Diego, CA 92121; [b]Center for Bioengineering and Tissue Regeneration, Department of Surgery, University of California San Francisco, San Francisco, CA 94143; [c]Structural Image Analysis Unit and [d]Structural Studies of Macromolecular Machines in Cellulo Unit, Institut Pasteur, CNRS UMR3528, Université de Paris Cité, F-75015 Paris, France

ABSTRACT **Matrix stiffness and dimensionality have been shown to be major determinants of cell behavior. However, a workflow for examining nanometer-scale responses of the associated molecular machinery is not available. Here, we describe a comprehensive, quantitative workflow that permits the analysis of cells responding to mechanical and dimensionality cues in their native state at nanometer scale by cryogenic electron tomography. Using this approach, we quantified distinct cytoskeletal nanoarchitectures and vesicle phenotypes induced in human mammary epithelial cells in response to stiffness and dimensionality of reconstituted basement membrane. Our workflow closely recapitulates the microenvironment associated with acinar morphogenesis and identified distinct differences in situ at nanometer scale. Using drug treatment, we showed that molecular events and nanometer-scale rearrangements triggered by engagement of apical cell receptors with reconstituted basement membrane correspond to changes induced by reduction of cortical tension. Our approach is fully adaptable to any kind of stiffness regime, extracellular matrix composition, and drug treatment.**

Monitoring Editor
Alex Dunn
Stanford University

Received: Mar 14, 2022
Revised: Oct 13, 2022
Accepted: Oct 19, 2022

This article was published online ahead of print in MBoC in Press (http://www.molbiolcell.org/cgi/doi/10.1091/mbc.E22-03-0092) on October 26, 2022.

Competing financial interests: The authors declare no competing financial interests.

†Present address: Department of Chemistry and Biochemistry and Department of Biomedical Engineering, University of California, Santa Barbara, CA 93106

Author contributions: D.H. and G.G. conceived and designed the CLEM, cryo-TEM, and cryo-ET workflow employed here, with assistance from M.F.S., F.B.K., and V.M.W. and feedback from N.V. N.V. pursued image processing, data analysis, and real-time quality control with feedback from G.G., M.F.S., and D.H. D.H., N.V., and G.G. wrote the manuscript with input from all authors.

*Address correspondence to: Dorit Hanein (dorit@ucsb.edu); Guido Gaietta (ggaietta@scintillon.org); Niels Volkmann (niels.volkmann@pasteur.fr).

Abbreviations used: 3D, three-dimensional; CLEM, correlative light and electron microscopy; cryo-EM, cryogenic electron microscopy; cryo-ET, cryogenic cellular tomography; cryo-MATE, cryogenic tunable matrix cellular electron tomography workflow; ECM, extracellular matrix; EM-grid, electron microscopy–compatible sample support; LM, light microscopy; rBM, reconstituted basement membrane ECM.

INTRODUCTION

Cells sense and transduce cues from the extracellular matrix (ECM) that are critical for regulating their behavior. The biochemical composition, organization, and mechanical properties of ECM all contribute to modulating cell growth, survival, migration, and differentiation to regulate tissue development and maintain homeostasis. A crucial aspect of mechanotransduction is the force-dependent alteration of the cell's nanometer-scale structural landscape and its translation into cellular signals (Katsumi *et al*., 2004; Schwartz, 2010; Ross *et al*., 2013; Humphrey *et al*., 2014; Sun *et al*., 2016; Ohashi *et al*., 2017).

Many experimental setups explore cellular responses to changes in the cellular microenvironment by employing gel-based ECM substrates. Two- and three-dimensional ECM model systems with tunable stiffness were developed to study the impact of ECM composition, stiffness, and dimensionality on cell phenotype (Tse and Engler, 2010; Shinsato *et al*., 2020). These model systems were coupled with molecular and pharmacological manipulations to identify key regulators of mechanotransduction (Pelham and Wang, 1997; Wang and Pelham, 1998; Kai *et al*., 2021) and used to examine the impact of ECM stiffness on oncogenic transformation (Paszek *et al*., 2005).

While these setups can report on general morphological changes detectable by light microscopy (LM), force-induced rearrangements of membrane topology and nanoarchitecture are achieved through conformational changes in the participating molecules and cytoskeletal elements.

To study these events in detail requires in situ information at the nanometer scale. The primary method for nanometer-scale in situ imaging is cryogenic cellular tomography (cryo-ET) (Asano *et al.*, 2016; Beck and Baumeister, 2016; Turk and Baumeister, 2020). Most cryo-ET studies on mammalian cells grow cells directly on an electron microscopy (EM)–compatible sample support (EM-grid), where only the basal portion interacts with EM-grid coatings such as fibronectin or collagen (Hampton *et al.*, 2017). Thin coatings with single proteins are not very accurate approximations of real live ECM. Mammalian cells in tissues interact with three-dimensional (3D) surroundings, where the entirety of the cell surface engages with the ECM. Thus, combining these model ECM systems with cryo-ET would present an ideal tool for investigating the molecular mechanisms underlying organ morphogenesis in health and disease.

However, cells in the presence of tunable ECM substrates are not directly amenable to cryo-ET owing to the thickness of ECM model systems, typically on the order of many micrometers (Mullen *et al.*, 2015), severely compromising cryo-ET imaging (Peet *et al.*, 2019) and vitrification (Dubochet, 2012). To overcome these challenges, we developed a novel, quantifiable workflow, **cryo**genic tunable **MAT**rix cellular **E**lectron tomography workflow (cryo-MATE), that merges ECM models of tunable stiffness, dimensionality, and composition with cryo-ET. The workflow is cell-type independent and can be combined with drug treatment.

Cryo-MATE allowed us to recapitulate cellular microenvironments associated with acinar morphogenesis closely and to reveal nanometer-scale changes in response to variations of the cellular microenvironment of cells from the human mammary epithelial cell line MCF-10A MEC (Soule *et al.*, 1990). MECs recap many aspects of mammary architecture in vivo when cultured in compliant 3D reconstituted basement membrane ECM (rBM) (Rubashkin *et al.*, 2014) and assemble into growth-arrested, apoptosis-resistant spheroids, secrete and assemble an endogenous basement membrane, and express tissue-specific differentiated gene expression (Streuli *et al.*, 1991; Debnath *et al.*, 2003; Imbalzano *et al.*, 2009). When MECs are cultured in stiffer, noncompliant 3D ECM, they start to exhibit invasive behavior (Rubashkin *et al.*, 2014). However, a 2D rBM fails to support 3D spheroids or endogenous basement membrane formation. Why MEC spheroids require interactions in 3D is poorly understood.

Using cryo-MATE, we identified distinct, statistically significant changes of actin cytoskeletal nanoarchitectures and vesicle phenotypes in situ in MECs occurring in response to physiological differences of ECM stiffness similar to those encountered in the transition from healthy to tumorous tissue. We showed that engagement of apical cell receptors with rBM, a condition that has recently been shown to recapitulate all hallmarks of a 3D environment in the context of organoid formation (Karzbrun *et al.*, 2021), triggers significant changes at the nanoscale if compared with 2D culture conditions. Using drug treatment, we showed that the nanometer-scale rearrangements triggered by this transition from a 2D to a 3D environment correspond to changes induced by reduction of cortical tension in the 2D environment.

RESULTS

The major obstacle to applying high-resolution cryo-ET coupled to ECM model systems is that their combined thickness exceeds the thickness amenable to cryo-ET imaging and plunge freezing. Thicker samples can be vitrified through high-pressure freezing, then thinned with cryogenic focused–ion beam (cryo-FIB) technology, and then physically manipulated to attach to an EM-grid (lift out). However, this process is generally involved and experimentally highly complex (Schaffer *et al.*, 2019) and has not been established for samples involving ECM model systems.

Our workflow allows cells to sense the stiffness, composition, and dimensionality of ECM model systems while keeping the sample thickness small, so that it is amenable to plunge freezing and high-resolution cellular cryo-ET. We focused on regions near the cell periphery that were thin enough for direct cryo-ET imaging, but cryo-MATE allows easy inclusion of well-established on-grid cryo-FIB technology for sample thinning (Rigort and Plitzko, 2015) if thicker cell regions need to be accessed.

Workflow concept and design

Cryo-MATE comprises of two preparation modules: 1) a hydrogel pad of tunable stiffness (Figure 1A) and 2) an EM-grid that is coated or patterned with ECM (Figure 1B). After placing the EM-grid directly on top of the hydrogel (Figure 1C), cells are plated on EM-grids and allowed to adhere. The basal membrane is then engaged with the coating as commonly practiced in 2D cell culture. To emulate 3D environments, jellifying solution of reconstituted ECM is added directly on top of the cells, allowing the apical cell membrane and its receptors to engage with the ECM.

We used Matrigel to emulate the ECM environment on the EM-grids. Matrigel is a heterogenous mixture of laminin, nidogen, collagen, heparan sulfate proteoglycans, and growth factors that mimics the endogenous basement membrane in tissues (Kleinman and Martin, 2005), and a thin layer of Matrigel triggers a transition from 2D culture to a 3D pluripotent monolayer epithelium in the context of in vitro neural tubulogenesis (Karzbrun *et al.*, 2021). Other types of ECM model systems such as tissue matrix gels or matrices directly extracted from cultured cells (Shinsato *et al.*, 2020) can be used instead of rBM in the workflow.

In the first module of cryo-MATE (Figure 1A), hydrogel pads are cast between two glass coverslips, one that is modified to couple to the polymerizing gel, and the other rendered nonsticky so that it can be peeled away easily from the coverslip after the polymerization process is completed (Przybyla *et al.*, 2016). In the second module (Figure 1B, C), EM-grids are separately prepared, including sterilization by shortwave UV light and coating with rBM or other reconstituted ECM. At this stage, patterning approaches can be employed to emulated spatial constraints of cell growth (Engel *et al.*, 2019; Toro-Nahuelpan *et al.*, 2020).

Next, the EM-grids are placed directly on top of the hydrogel pads and adherent cells are plated on the EM-grids (Figure 1C). Because of the soft PA hydrogel's poroelasticity and tendency to swell once immersed in media, direct contact between the basal cell surface and the underlying substrate is established through the holes in the holey carbon film on the EM-grids. In addition, there is mechanical coupling through the relatively soft, thin carbon film, allowing the cells to sense the hydrogel indirectly everywhere else. We use 30-mm dishes or six-well plates when combining the two modules. These vessels offer the best compromise between total volume and ability to safely manipulate the EM-grid, allowing to approach it at a 45° angle to lift it more easily from the hydrogel with minimal damage.

After removal from the hydrogel, the EM-grid can be directly plunge-frozen or viewed by LM (Figure 1D). Correlating cryo-ET with functional states requires linking to LM for studying dynamics and

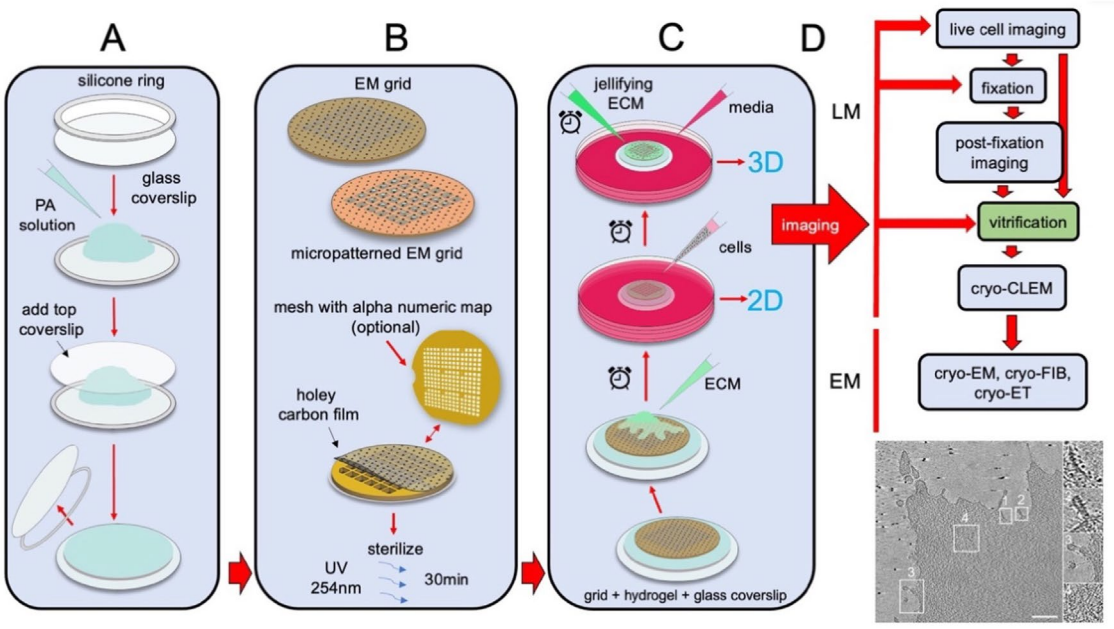

FIGURE 1: Cryo-MATE workflow design. (A) PA hydrogels of the desired elastic module and composition are polymerized on glutaraldehyde-modified glass coverslips, using a silicone ring to obtain a specific gel thickness; before the EM grid is applied on top of the hydrogel, ring and top coverslips are removed. (B) Gold grids are used as EM substrate and may be modified by applying micropatterns to the carbon foil surface to emulate in vivo spatial constraint; EMBRA finder grids are particularly useful in correlated studies thanks to their alphanumeric map of lettered regions A–I, each numbered 1–24. Before use, grids are sterilized by exposure to a 254-nm UV light source for 30 min. (C) The sterilized EM grid is placed on top of the hydrogel and then coated with the reconstituted ECM of choice. Cells are plated at this point and can be further processed directly (2D condition). An additional thin layer of reconstituted ECM can be added on top of the cells to completely encase them in the reconstituted ECM and emulate a 3D condition. (D) Cells can be vitrified directly or can be imaged live until the desired time point is reached, and then fixed to block any biological activity. If no live imaging is necessary but correlative LM is required, cells can be fixed and then examined to record the position of a specific fluorescent reporter or taken directly to vitrification without fixation. Once vitrified, cells can be further imaged using a cryo-CLEM set up and/or processed for cryo-EM and cryo-ET. Cryo-FIB can also be employed to investigate thicker regions of the sample by cutting thin lamellae. The insets in the bottom right are from a 2 nm–thick slice of a tomogram (scale bars, 200 nm).

function and localization of regions of interest. In this correlative light and electron microscopy (CLEM) workflow, cells are vitrified once the LM study of choice is completed (Sartori *et al.*, 2007; Schwartz *et al.*, 2007), before proceeding to cryo-ET. If live-cell imaging is performed, fixative can be applied once the imaging session is completed to halt progression of all cellular functions that would otherwise jeopardize the correlation between LM and EM modalities (Gaietta *et al.*, 2021). In our hands, manual plunge freezing provides the best vitrification of cells and preservation of EM-grid integrity. For correlative analysis, precise alignment can be achieved using features of the EM-grids (Anderson *et al.*, 2018). For samples where cellular function does not need to be blocked and where no pathogens need to be inactivated, fixation can be omitted.

Cryo-MATE is compatible with imaging high-resolution cellular nanoarchitecture

We used MCF-10A nonmalignant human MECs (Soule *et al.*, 1990) to validate that the two modules of cryo-MATE are compatible with cell adhesion, growth, imaging, vitrification, and high-resolution cryo-ET. To facilitate the identification of membrane protrusions, we used a farnesylated form of Emerald GFP (Rubashkin *et al.*, 2014). MECs assemble polarized, growth arrested spheroids when embedded within a 3D compliant ECM (Petersen *et al.*, 1992), analogous to the structures observed in normal compliant human breasts. However, when embedded within an ECM with stiffness similar to that of human breast tumors, MECs form large, continuously growing, nonpolarized colonies with individual cells in the periphery probing into the surrounding ECM with prominent protrusions (Rubashkin *et al.*, 2014), indicative of the initiation of cancer cell migration (Meyer *et al.*, 2012). MECs, when paired with polyacrylamide (PA) hydrogels of tuned (healthy to tumor) stiffness, not only offer an attractive experimental paradigm to study the impact of mechanical cues on cellular cytoskeletal architecture and membrane organization but also provide an ideal testbed for validation of our approach.

The validation process involved the comparison between a stripped-down benchmark condition commonly used for 2D cell culture aiming at cryo-ET, where cells were plated on the bare carbon film of EM-grids (Figure 2, A–F), and a modified condition corresponding to our workflow where we introduced a few significant variables: 1) coating the EM-grid's carbon film with rBM, mimicking the endogenous basement membrane ECM with which MECs interact within tissues in vivo; 2) positioning the EM-grid on a very soft PA hydrogel with a physiologically relevant compliant elastic modulus of 75 Pa, mimicking the normal compliance of human breasts; and 3) treating the cells with the drug Blebbistatin, a myosin-II inhibitor that is frequently used to reduce cortical tension (Fischer *et al.*, 2009; Chugh *et al.*, 2017; Figure 2, G–L).

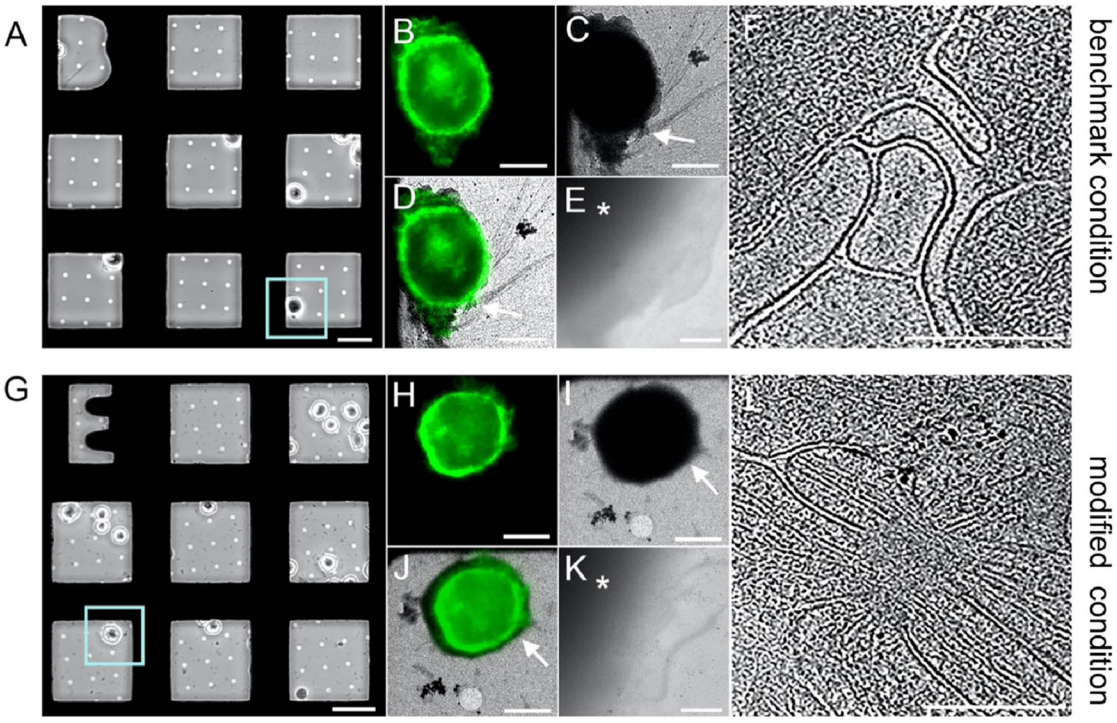

FIGURE 2: Cryo-MATE workflow validation: the preparation modules are compatible with cell adhesion, growth, imaging, vitrification, and cryo-EM/ET. We used MCF-10A cells expressing a farnesylated form of EGFP for cell surface demarcation and tested two conditions to validate our workflow: a benchmark condition, A–F, with cells plated on the bare carbon film of the EM grid and a modified condition, G–L, with cells plated on a rBM-coated grid placed on top of a compliant (75-Pa) hydrogel and subjected to treatment with the myosin II inhibitor Blebbistatin. The blue squares in A and G indicate the cell chosen for the validation experiment (cells in Embra grid positions B12 and E2, respectively). CLEM images were collected and compared for each cell (B, H, fluorescence images; C, I, cryo-EM images; D, J, overlay of the fluorescence and cryoEM images to help delineate the cell area displaying the EGFP reporter; E, K, cryo-EM overviews of the cell area chosen for cryo-ET (white asterisks in E and K mark the position of the cell body); F, L, 2 nm–thick slice from a tomogram taken of the area of interest. As shown in the images, the grid and cells in the modified condition behaved similarly to those in the benchmark condition, with no loss in carbon-layer integrity, cell adhesion, or preservation of the ultrastructure. Scale bars, A, G, 40 μm; B, C, D, H, I, J, 10 μm; E, K, 1 μm; F, I, 200 nm.

Cells in both conditions were incubated for 1 h at 37°C in a humidified incubator and successfully adhered to the substrate in a similar manner. After nonadherent cells were gently removed with a phosphate-buffered saline (PBS) rinse, cells in the benchmark condition were fixed, while those in the modified condition were placed back in growth media and treated for an additional hour with Blebbistatin and then fixed. The EM-grid integrity in the modified condition after lifting off from the hydrogel was comparable to that in the benchmark condition (Figure 2, A and G). Samples were manually vitrified and proceeded to assess its overall quality. Following screening to ensure retention of sample preservation and morphology, areas of interest were identified via CLEM (Figure 2, B–E, H–K). The fluorescent signal was overlaid with the cryo-EM image of each target area to collect tomographic tilt series (Figure 2, D and J). The quality of preservation and detail in the tomographic reconstructions from our modified condition is excellent and comparable to that seen under the benchmark condition (Figure 2, F and L), corroborating that our workflow can be applied successfully to live cells and is fully compatible with CLEM and cryo-ET investigations.

MCF-10A mammary epithelial cells sense the stiffness of the underlying substrate

Once our protocol was validated, we applied it to determine the nanometer-scale changes in MECs triggered by different stiffness regimes ("stiff"; glass, elastic modulus 69×10^9 Pa vs. "soft"; a compliant PA hydrogel, elastic modulus 75 Pa) We targeted single, nonspread MECs during the early stages of adhesion to exclude potential contributions from cell–cell junctions and multicellularity. Four experimental conditions were tested: bare^{stiff}; bare^{soft}; rBM^{stiff}; rBM^{soft}—cells plated on EM-grids with bare carbon film (bare) or coated with rBM (rBM), with the EM-grid placed either on glass (^{stiff}) or on a 75-Pa hydrogel (^{soft}). We quantified the protrusion width and the percentage of filled versus empty intracellular membrane compartments for each condition.

Statistical evaluation revealed a highly significant difference for both quantifications when stiff conditions were compared with soft conditions (Figure 3). Thus, cells change their nanoscale architecture in response to stiffness of the substrate underneath the EM-grid independent of whether it is coated with rBM. The stiff surfaces triggered the formation of a busy landscape of often interwoven actin-based protrusions in MECs that appear as irregular cell edges at lower magnification (Supplemental Figure S1). The protrusions were short and wide under the bare^{stiff} condition, and more elongated under the rBM^{stiff} condition. The soft condition encouraged a less crowded landscape, with either relatively short protrusions or long, isolated protrusions. This effect was independent of whether the carbon was coated with rBM.

For intracellular membrane-enclosed compartments, the phenotypes are more subtle and visually less noticeable. However, when the statistics are compiled, the difference becomes apparent

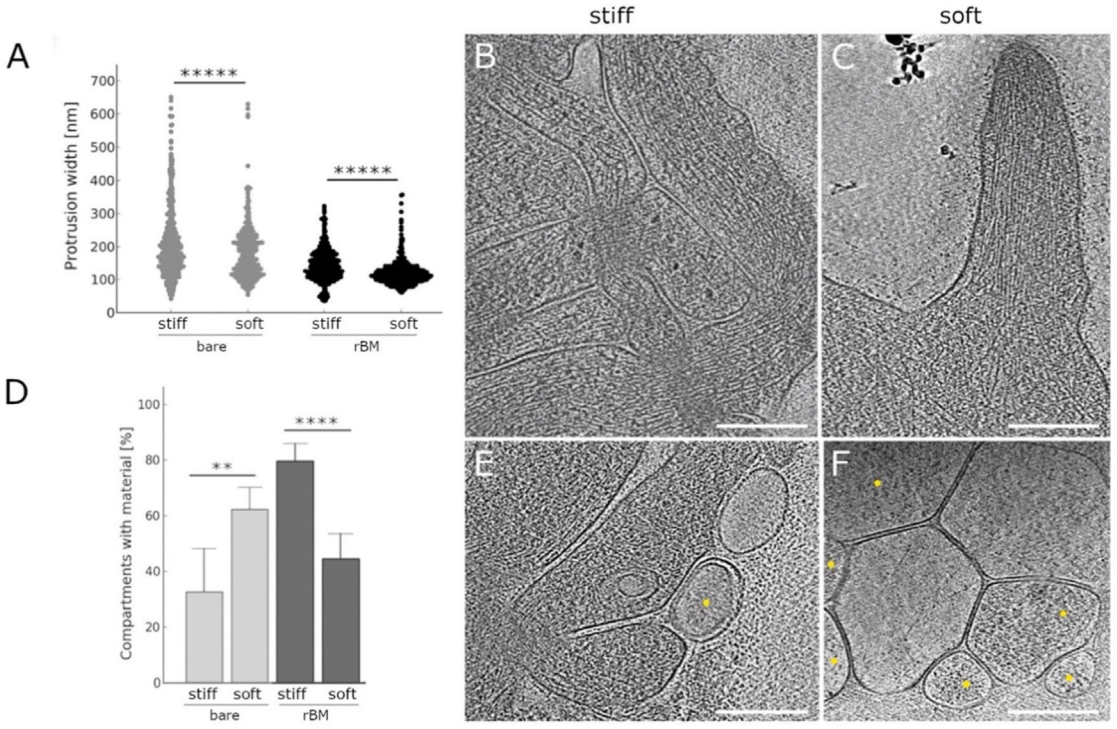

FIGURE 3: MCF-10A MECs sense the stiffness of the substrate underneath the EM grid and change their nanoscale architecture accordingly. (A) The statistical differences between the distributions of protrusion widths comparing cells adhered to grids placed on glass (bare^{stiff} and rBM^{stiff} conditions) or on a PA hydrogel of 75Pa elastic module (bare^{soft} and rBM^{soft} conditions) are highly significant, regardless of whether cells were plated on bare carbon or on rBM-coated carbon (see Supplemental Table S1 for significance levels and p-values). (B, C) Slices 2 nm thick through representative tomograms of cells plated on bare carbon under the stiff, B, and soft, C, conditions. Scale bars are 200 nm. (D) The statistical differences between the relative percentages of filled intracellular membrane-enclosed compartments when cells under the stiff and soft conditions are compared are highly significant, regardless of whether cells were plated on bare carbon or on rBM-coated carbon (see Supplemental Table S2 for significance levels and *p*-values). (E, F) Slices 2 nm thick through representative tomograms of cells plated on bare carbon under the stiff, E, and soft, F, conditions. Filled intracellular membrane-enclosed compartments are marked by yellow dots. Scale bars, 200 nm.

(Figure 3D). Interestingly, the percentage of filled intracellular membrane-enclosed compartments approximately doubles from bare^{stiff} to bare^{soft} (32.5 ± 14.3% vs. 62.1 ± 7.7%). However, the percentage of filled intracellular membrane-enclosed compartments is cut approximately in half from rBM^{stiff} to rBM^{soft} (79.5 ± 6.6% vs. 44.4 ± 9.6%). These reverse trends demonstrate that the type of ECM presented to the basal membrane of the cells has a clear impact on nanoscale cellular topology. Indeed, a comparison of the rBM^{stiff} condition with cells plated on grids placed on glass and coated with the ECM protein laminin, a component of the rBM (Supplemental Figure S2), shows that the exact composition of the ECM can be a critical determinant of MCF-10A MEC nanomorphology.

MCF-10A mammary epithelial cells respond to the dimensionality of the microenvironment similarly to artificially reduced cortical tension

Next, we investigated changes induced by the dimensionally of rBM engagement. To emulate aspects of a 3D environment, cells under the rBM^{soft} condition (rBM^{2D}) were encased with a thin layer of jellified rBM (rBM^{3D}), allowing apical membrane receptors to engage with rBM. In the rBM^{2D} environment, only basal receptors can engage with rBM. The difference between rBM^{2D} and rBM^{3D} is statistically highly significant for both percentage of filled intracellular membrane-enclosed compartments (44.4 ± 9.6% vs. 72.8 ± 7.9%) and actin-based protrusions (Figure 4), confirming that the dimensionality of the microenvironment has a significant effect on cellular nanoarchitecture.

Because myosin II function is intimately involved with cell responses to dimensionality, we treated MECs under the rBM^{2D} condition with Blebbistatin (rBM^{Blebb}). Blebbistatin inhibits myosin II, reducing the cortical tension. Interestingly, there was no statistically significant difference between the quantifications if rBM^{3D} and rBM^{Blebb} were compared (Figure 5) for both actin protrusions (p = 0.089) and percentage of filled intracellular membrane–enclosed compartments (62.9 ± 11.1% vs. 72.8 ± 7.9%). Thus, the reduction of cortical tension and the transition from 2D to 3D ECM environments have approximately the same effect on the nanoarchitecture of MECs. For both rBM^{3D} and rBM^{Blebb}, the number of long, interwoven, nondirectional protrusions was appreciably greater than under the bare^{stiff}; bare^{soft}; rBM^{stiff}; and rBM^{2D} conditions. The protrusion widths shifted to higher values (Figures 4A, 5A) and the percentage of filled intracellular membrane-enclosed compartments increased significantly compared with rBM^{2D} (Figures 4D, 5D). The latter indicates that there might be an increase in membrane trafficking if the rBM^{2D} is compared with the rBM^{3D} or rBM^{Blebb} condition.

DISCUSSION

The Cryo-MATE workflow fills a void amongst current approaches to studying mechanotransduction by providing a means to study the macromolecular organization in the cell response to matrix

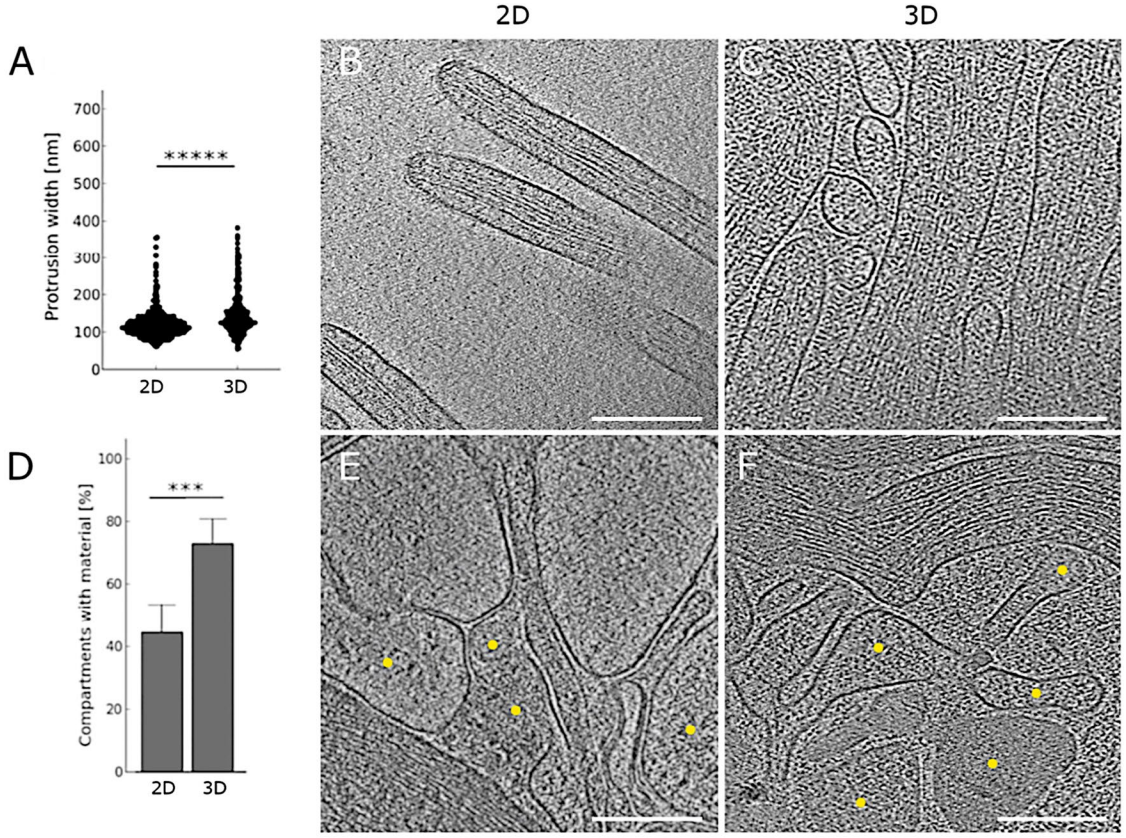

FIGURE 4: MCF-10A MECs respond to the dimensionality of the microenvironment. (A) The statistical difference between the distributions of protrusion widths comparing cells adhered to rBM-coated grids (2D; rBM^{soft}/rBM^{2D} condition) and cells encased with rBM (3D; rBM^{3D} condition) is highly significant (see Supplemental Table S1 for significance levels and *p*-values). (B, C) Slices 2 nm thick through representative tomograms of cells under rBM^{2D}, B, and rBM^{3D}, C, conditions. Scale bars are 200 nm. (D) The statistical difference between the relative percentages of filled intracellular membrane-enclosed compartments when cells under rBM^{2D} and rBM^{3D} conditions are compared is highly significant (see Supplemental Table S2 for significance levels and *p*-values). (E, F) Slices 2 nm thick through representative tomograms of cells under rBM^{2D}, E, and rBM^{3D}, F, conditions. Filled intracellular membrane-enclosed compartments are marked by yellow dots. Scale bars, 200 nm.

composition, dimensionality, and stiffness with nanometer resolution. By splitting the workflow into two individual preparation modules, we bypass requirements for additional hardware and complex experimental procedures necessary for investigating thick samples by cryo-ET, a workflow that is in its infancy (Schaffer *et al.*, 2019). Our platform is easily adaptable to specific experimental requirements including hydrogel composition, geometry, elastic modulus, ECM coating, cell type, and growth times (Supplemental Figure S3). Our workflow enables quantification of nanometer differences between cells in 3D and 2D environments as well as the effects of different substrate stiffness regimes, ECM compositions, and drug treatments.

Stiffness can be modulated by adjusting the composition of the hydrogel, mimicking in vitro the physiological and pathological dynamic remodeling of ECM in vivo. For example, an increase in stiffness of the ECM, as often observed in fibrotic tissue, causes an aberrant engagement in the cellular mechanosignaling networks, which then promotes the assembly of actin-rich invadosomes and lamellae for cell invasion and migration (Kai *et al.*, 2016; Bisaria *et al.*, 2020). Previous studies used hydrogels with tunable stiffness to demonstrate that a stiffer substrate significantly enhanced cell migration (Pelham and Wang, 1997). Our method now offers a way to follow the dynamic changes in these actin-rich structures at nanometer resolution.

Hydrogels can be formulated with any given geometry and modulus, two factors known to affect the structural stiffness sensed by the cell (Maloney *et al.*, 2008; Sen *et al.*, 2009; Mullen *et al.*, 2015). When hydrogels are presented as a separate module, their thickness is no longer an obstacle for vitrification or for cryo-ET imaging and hence can be adjusted freely according to the experimental design. It was shown that for soft hydrogels with thickness below 5 µm, cell behavior is influenced by the underlying stiff substrate that supports the gel (Mullen *et al.*, 2015), so being able to increase hydrogel thickness is crucial. The hydrogel scaffold in the workflow is interchangeable. For instance, it would be possible to use a gel with a better refractive index than PA, such as silicone gels (Ou *et al.*, 2016).

Although PA hydrogels are prepared through a relatively lengthy process, once assembled they can be stored in hydrated form at 4°C for weeks. We prefer to prepare EM-grids on the day of the experiment, with sterilization and ECM coating completed within a couple of hours. Overall, when premade hydrogels and freshly treated grids are combined, the assembly of the two modules is relatively quick and efficient.

Cryo-MATE is designed to unravel high-resolution details of cell responses to changes in their extracellular environment, specifically as they relate to stiffness, composition, and dimensionality. Thus,

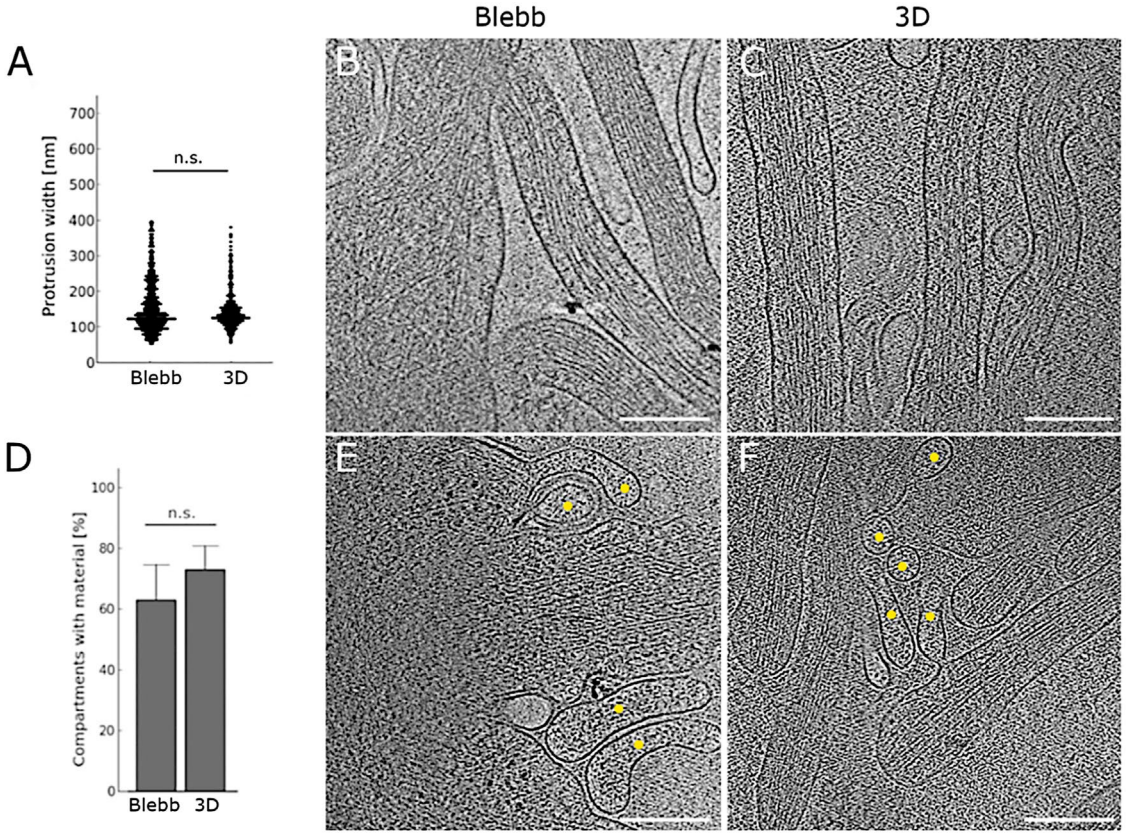

FIGURE 5: MCF-10A MECs respond to the dimensionality of the microenvironment similarly to artificially reduced cortical tension. (A) The statistical difference between the distributions of protrusion widths comparing cells adhered to rBM-coated grids treated with Blebbistatin (Blebb; rBM^{Blebb} condition) and cells encased with rBM (3D; rBM^{3D} condition) is not significant (see Supplemental Table S1 for significance levels and *p*-values). (B, C) Slices 2 nm thick through representative tomograms of cells under the Blebb, B, and 3D, C, conditions. Scale bars are 200 nm. (D) The statistical difference between the relative percentages of filled intracellular membrane-enclosed compartments when cells under the rBM^{Blebb} and rBM^{3D} conditions are compared is not significant (see Supplemental Table S2 for significance levels and *p*-values). (E, F) Slices 2 nm thick through representative tomograms of cells under the rBM^{Blebb}, E, and rBM^{3D}, F, conditions. Filled intracellular membrane-enclosed compartments are marked by yellow dots. Scale bars, 200 nm.

the workflow is particularly well suited to investigate cells that may eventually be used to generate organoids in 3D models and that are known to respond well to biomechanical stimuli. We applied our workflow to MCF-10A MECs because they display features characteristic of nonmalignant cells, recapitulating many aspects of mammary architecture when cultured in 3D rBM. They maintain a near-diploid karyotype, modest genetic modifications, and inability to grow in immune-compromised mice (Soule *et al.*, 1990; Heppner and Wolman, 1999; Debnath *et al.*, 2002, 2003). They offer an appealing model for tumor progression, as premalignant (Dawson *et al.*, 1996) and fully malignant (Santner *et al.*, 2001) lines are available. In conjunction with Blebbistatin treatment for myosin II inhibition, the workflow deciphered the relationships between cortical tension, dimensionality sensing, and substrate stiffness in MECs. The differences we observed between 2D and 3D conditions and the recapitulation of these differences with Blebbistatin treatment are consistent with the idea that ECM engagement may influence protein secretion by modulating cortical actin tension to regulate plasma membrane topology (Kai *et al.*, 2021), underscoring the importance of ECM in the regulation of organelle homeostasis and tissue phenotype. This difference between 2D and 3D conditions may help explain why organoids cultured within a 3D rBM but not in 2D are able to faithfully reconstitute self-organization phenotypes and tissue behaviors such as branching morphogenesis and tubulogenesis (Karzbrun *et al.*, 2021).

Cryo-MATE is easily expandable to other adherent cell types and incubation times can be adjusted. Longer culture times make it possible to apply the workflow to more complex culture systems such as organoids and to address questions regarding cell polarity, differentiation, and tissue morphogenesis at a much higher resolution than previously available. Given that metastatic cancer cells interact with 3D ECMs of various stiffness regimes throughout the metastatic cascade, the workflow developed here allows molecular-detailed characterization of cancer progression in 3D ECM landscapes.

MATERIALS AND METHODS

Cell culture

The human mammary gland, epithelial cell line MCF-10A, was a generous gift from T. Tlsty (UCSF). To generate the stable cell line hPGK-CAAX-Emerald, MCF-10A cells were cotransfected with a lentiviral vector containing the farnesylated Emerald sequence along with the viral packaging plasmids (psPAX and pMD2.G). The lentiviral vector was first expressedin HEK293T cells. The supernatant was collected 48 h posttransfection, and cell debris along with HEK293T cells was removed by centrifugation. The virus-containing supernatant was supplemented with 4 μg/ml polybrene and added

to MCF10A cells. Cells were infected with lentivirus carrying the indicated constructs for 24 h and cultured for another 24 h with fresh growth medium before selection with puromycin or neomycin. Dead cells and debris were periodically removed by replenishing the monolayer with selection medium.

Polyacrylamide compliant gels

Glass coverslips (Deutsch Deckglasern, Neuvitro; we used either 20-mm or 12-mm coverslips, depending on the type of well used when seeding cells) were coated with acrylamide-bis-acrylamide to generate 75Pa gels. Polyacrylamide gels were first polymerized on glutaraldehyde-modified glass coverslips. Gels were equilibrated in serum-free media at 37°C for at least 4 h before cell seeding and may be stored in the same at 4°C for up to a week. It is important to note that the hydrogel pads were not functionalized, as the coating with an ECM constituent, when needed, was shifted to the second module of our workflow and applied directly to the EM grid. Once we were ready to start the assay, we placed these gels in the appropriate vessel (30-mm dishes or six-well plates for 20-mm coverslips, 12-well plates for 12-mm coverslips) and used them in the following steps.

Holey carbon coated gold finder electron microscopy–compatible sample supports: preparation and coating

Two hundred–mesh R5/20 holey carbon–coated gold finder grids (Quantifoil) were sterilized for 30 min on each side using a UV source (shortwave germicidal UV bulb, 254 nm) placed at about 3–8″ from grids. Grids were then gently positioned directly on top of the acrylamide-bis-acrylamide gel, carbon film side up. Care must be taken from this moment on not to allow the grids to go dry, as this may cause cracking and tears in the holey-carbon support film. When required, grids were coated with Matrigel suspended in ice-cold 100-mM HEPES, 100-mM NaCl, pH 8.0 at varying concentrations (1:200, 25%, and 50%) O/N at 4°C on a shaker. If not used immediately, treated grids were maintained in sterile phosphate-buffered solution at 4°C.

Cell seeding

MECs in log phase were gently detached using a 0.05% solution of trypsin as suggested for this specific cell line and centrifuged at 700 × *g* for 5 min upon addition of 20% horse serum. The cell pellet was then resuspended in complete growth medium and cells were counted and diluted according to the experimental requirements. Upon plating onto each 30-mm dish containing the two modules, cells were incubated in a humidified incubator for the desired time, and then nonadhered cells were removed by gentle washing with 1× PBS.

Treatment with Blebbistatin

Cells seeded as described above were allowed to attach to grids for 1 h at 37°C in a humidified incubator. After cells that did not attach were removed by gently washing with warm PBS, a 1:2000 dilution of the Blebbistatin stock in medium was applied to obtain a final concentration of 4 µM. As the Blebbistatin stock solution is prepared in DMSO, a 1:2000 dilution of DMSO in media was used as negative control (mock). Cells were incubated in the presence of Blebbistatin or mock for an additional hour at 37°C in a humidified incubator. Upon examination, cells treated with the DMSO solution (mock) did not show any significant difference from untreated cells.

Fixation and light microscopy

Following the indicated adhesion and treatment times, cellular activity was halted via rapid fixation using the buffer conditions determined with the RCIA protocol (Gaietta *et al.*, 2021). In brief, a solution of 4% formaldehyde, 0.1 M Pipes, 1 mM EGTA, and 1 mM $MgSO_4$, pH 6.9, was applied for 30 min at 37°C. The fixative was removed by a quick wash in room temperature PHEM (60 mM Pipes, 25 mM HEPES, 2 mM $MgSo_4$, 10 mM EGTA, pH 6.9 followed by three times, 3 min each wash, in room-temperature PHEM buffer. The samples were imaged on an inverted light microscope (Eclipse TE 2000-U, Nikon) equipped with manual controlled shutter, filter wheels, and a 14-bit cooled CCD camera (Orca II) controlled by MetaMorph software (Universal Imaging), using a Plan Fluor ELWD 40/0.60 Ph2 or a Plan Fluor 10/0.30 Ph1 objective lens (Nikon). The samples were vitrified by manual plunge-freezing in liquid nitrogen–cooled liquefied ethane to prevent structural collapse or shrinkage associated with dehydration. The vitrification was done using a home-designed cryoplunger. If required, the samples were store at 4°C before vitrification.

Correlative light and cryo-electron microscopy

The fluorescent images collected after fixation and before vitrification were precisely aligned with images of the same cells obtained by cryo-EM, using a fiducial-less approach (Anderson *et al.*, 2018). Briefly, this approach is based on the visibility of holes in the carbon support in both imaging modalities. While they are readily identifiable in the cryo-EM images, holes are not always apparent in the fluorescent images. To overcome this obstacle, we increased the contrast to maximum and suppressed noise with iterative median filtering or, in cases of higher noise levels, nonlocal means, bilateral filtering, or anisotropic nonlinear diffusion. Once the hole center locations are determined, a one-to-one correspondence mapping between holes in the two imaging modalities is determined. The coordinates are then used to determine rotation, translation, and relative scale between fluorescence and cryo-EM images.

Cellular cryo-tomography and image/volume processing

Electron cryo-tomography data were taken with a FEI Titan Krios equipped with an extra–high brightness field emission gun (XFEG) and operated at 300 kV. Tilt series (± 65°, every 1.5°) were acquired on the back-thinned 4k × 4k FEI Falcon II direct detection imaging device under minimal dose conditions using the Tomo package in batch mode (ThermoFisher Scientific; FEI Company) at an average dose of about 100–120 $e^{-}/Å^2$ and defocus of 8–15 µm, depending on the thickness of the sample. Real-time automatic reconstruction protocols were implemented in the pyCoAn package (github.com/pyCoAn/distro), an extended python version of the CoAn package (Volkmann and Hanein, 1999). Briefly, immediately after acquisition, tilt series were automatically aligned using patch tracking (Kremer *et al.*, 1996) and reconstructed using the simultaneous iterative reconstruction technique (Agulleiro and Fernandez, 2015). Alignment and reconstruction statistics were used to determine quality scores, which are provided in real time during data collection. Images of tomogram slices were generated with IMOD (Kremer *et al.*, 1996). We collected, reconstructed, and analyzed a total of 191 tomograms: 39 tomograms of samples plated on uncoated carbon placed on glass ($bare^{stiff}$), 34 plated on uncoated carbon placed on PA ($bare^{soft}$), 33 on carbon coated with Matrigel placed on glass (rBM^{stiff}), 38 on carbon coated with Matrigel placed on PA (rBM^{soft}, rBM^{2D}), 37 on carbon coated with Matrigel, placed on PA, and treated with Blebbistatin (rBM^{Blebb}) and 10 on carbon coated with Matrigel, placed on PA, and covered with a Matrigel layer (rBM^{3D}).

Statistical evaluation

Whether intracellular membrane-enclosed compartments were filled or not was assessed visually by assigning a score of 1 or 0 for each condition. The criteria were either clearly discernible particulate material or densely filled with smooth material in the compartments. The scoring was repeated three times independently by three different cryo-EM experts to compile the statistics. Forty-two membrane compartments were characterized for condition bare^{stiff}, 132 for bare^{soft}, 116 for rBM^{stiff}, 45 for rBM^{soft}, 70 for rBM^{Blebb}, and 92 for rBM^{3D}. Protrusion widths were measured every 200 nm along each protrusion in the tomograms. Seven hundred six measurements were done in the bare^{stiff} condition, 736 in bare^{soft}, 887 in rBM^{stiff}, 820 for rBM^{soft}, 713 in rBM^{Blebb}, and 403 in rBM^{3D}. Two-sided Kruskal–Wallis tests were used to test whether the membrane-content and protrusion-width data samples derived under the various conditions originated from the same respective distribution. In both cases, the statistics clearly indicated that the samples did not come from the same distribution ($p = 3.38 \times 10^{-14}$ for membrane content and $p = 3.36 \times 10^{-135}$ for protrusion widths). We then performed post hoc pairwise two-sided Mann–Whitney U tests with Bonferroni correction to determine the significance of differences between data samples from the individual conditions. The individual *p*-values and significance levels are listed in Supplemental Tables S1 and S2.

ACKNOWLEDGMENTS

This work was supported by the following grants: U.S. National Institutes of Health Grants R01-CA138818, R01-CA192914, R01-CA174929, R01-CA085482, R01-CA227942; and U01-CA202241 (V.M.W.); Canadian Institutes of Health Research Postdoctoral Fellowship (F.B.K.). The authors acknowledge the use of the Titan Krios, Tecnai Spirit T12, and auxiliary equipment at the cryo-EM unit of the Sanford Burnham Prebys Medical Discovery Institute, which was created in part with the support of U.S. National Institutes of Health Grant S10-OD012372 (D.H.) and Pew Charitable Trust 864K625 innovation award funds (D.H.).

REFERENCES

Agulleiro J-I, Fernandez J-J (2015). Tomo3D 2.0–exploitation of advanced vector extensions (AVX) for 3D reconstruction. J Struct Biol 189, 147–152.

Anderson KL, Page C, Swift MF, Hanein D, Volkmann N (2018). Marker-free method for accurate alignment between correlated light, cryo-light, and electron cryo-microscopy data using sample support features. J Struct Biol 201, 46–51.

Asano S, Engel BD, Baumeister W (2016). In situ cryo-electron tomography: a post-reductionist approach to structural biology. J Mol Biol 428, 332–343.

Beck M, Baumeister W (2016). Cryo-electron tomography: can it reveal the molecular sociology of cells in atomic detail. Trends Cell Biol 26, 825–837.

Bisaria A, Hayer A, Garbett D, Cohen D, Meyer T (2020). Membrane-proximal F-actin restricts local membrane protrusions and directs cell migration. Science 368, 1205–1210.

Chugh P, Clark AG, Smith MB, Cassani DAD, Dierkes K, Ragab A, Roux PP, Charras G, Salbreux G, Paluch EK (2017). Actin cortex architecture regulates cell surface tension. Nat Cell Biol 19, 689–697.

Dawson PJ, Wolman SR, Tait L, Heppner GH, Miller FR (1996). MCF10AT: a model for the evolution of cancer from proliferative breast disease. Am J Pathol 148, 313.

Debnath J, Mills KR, Collins NL, Reginato MJ, Muthuswamy SK, Brugge JS (2002). The role of apoptosis in creating and maintaining luminal space within normal and oncogene-expressing mammary acini. Cell 111, 29–40.

Debnath J, Muthuswamy SK, Brugge JS (2003). Morphogenesis and oncogenesis of MCF-10A mammary epithelial acini grown in three-dimensional basement membrane cultures. Methods 30, 256–268.

Dubochet J (2012). Cryo-EM—the first thirty years. J Microsc 245, 221–224.

Engel L, Gaietta G, Dow LP, Swift MF, Pardon G, Volkmann N, Weis WI, Hanein D, Pruitt BL (2019). Extracellular matrix micropatterning technology for whole cell cryogenic electron microscopy studies. J Micromech Microeng 29,

Fischer RS, Gardel M, Ma X, Adelstein RS, Waterman CM (2009). Local cortical tension by myosin II guides 3D endothelial cell branching. Curr Biol 19, 260–265.

Gaietta G, Swift MF, Volkmann N, Hanein D (2021). Rapid tool for cell nanoarchitecture integrity assessment. J Struct Biol 213, 107801.

Hampton CM, Strauss JD, Ke Z, Dillard RS, Hammonds JE, Alonas E, Desai TM, Marin M, Storms RE, Leon F, *et al.* (2017). Correlated fluorescence microscopy and cryo-electron tomography of virus-infected or transfected mammalian cells. Nat Protoc 12, 150–167.

Heppner GH, Wolman SR (1999). MCF-10AT: a model for human breast cancer development. Breast J 5, 122–129.

Humphrey JD, Dufresne ER, Schwartz MA (2014). Mechanotransduction and extracellular matrix homeostasis. Nat Rev Mol Cell Biol 15, 802–812.

Imbalzano KM, Tatarkova I, Imbalzano AN, Nickerson JA (2009). Increasingly transformed MCF-10A cells have a progressively tumor-like phenotype in three-dimensional basement membrane culture. Cancer Cell Int 9, 7.

Kai F, Laklai H, Weaver VM (2016). Force matters: biomechanical regulation of cell invasion and migration in disease. Trends Cell Biol 26, 486–497.

Kai F, Ou G, Tourdot RW, Stashko C, Gaietta G, Swift MF, Volkmann N, Long AF, Han Y, Huang HH, *et al.* (2021). ECM dimensionality tunes actin tension to modulate the endoplasmic reticulum function and spheroid phenotypes of mammary epithelial cells. EMBO J, in press.

Karzbrun E, Khankhel AH, Megale HC, Glasauer SMK, Wyle Y, Britton G, Warmflash A, Kosik KS, Siggia ED, Shraiman BI, *et al.* (2021). Human neural tube morphogenesis in vitro by geometric constraints. Nature 599, 268–272.

Katsumi A, Orr AW, Tzima E, Schwartz MA (2004). Integrins in mechanotransduction. J Biol Chem 279, 12001–12004.

Kleinman HK, Martin GR (2005). Matrigel: basement membrane matrix with biological activity. Semin Cancer Biol 15, 378–386.

Kremer JR, Mastronarde DN, McIntosh JR (1996). Computer visualization of three-dimensional image data using IMOD. J Struct Biol 116, 71–76.

Maloney JM, Walton EB, Bruce CM, Van Vliet KJ (2008). Influence of finite thickness and stiffness on cellular adhesion-induced deformation of compliant substrata. Phys Rev E Stat Nonlin Soft Matter Phys 78, 041923.

Meyer AS, Hughes-Alford SK, Kay JE, Castillo A, Wells A, Gertler FB, Lauffenburger DA (2012). 2D protrusion but not motility predicts growth factor-induced cancer cell migration in 3D collagen. J Cell Biol 197, 721–729.

Mullen CA, Vaughan TJ, Billiar KL, McNamara LM (2015). The effect of substrate stiffness, thickness, and cross-linking density on osteogenic cell behavior. Biophys J 108, 1604–1612.

Ohashi K, Fujiwara S, Mizuno K (2017). Roles of the cytoskeleton, cell adhesion and rho signalling in mechanosensing and mechanotransduction. J Biochem 161, 245–254.

Ou G, Thakar D, Tung JC, Miroshnikova YA, Dufort CC, Gutierrez E, Groisman A, Weaver VM (2016). Visualizing mechanical modulation of nanoscale organization of cell–matrix adhesions. Integr Biol (Camb) 8, 795–804.

Paszek MJ, Zahir N, Johnson KR, Lakins JN, Rozenberg GI, Gefen A, Reinhart-King CA, Margulies SS, Dembo M, Boettiger D, *et al.* (2005). Tensional homeostasis and the malignant phenotype. Cancer Cell 8, 241–254.

Peet MJ, Henderson R, Russo CJ (2019). The energy dependence of contrast and damage in electron cryomicroscopy of biological molecules. Ultramicroscopy 203, 125–131.

Pelham RJ, Wang Y (1997). Cell locomotion and focal adhesions are regulated by substrate flexibility. Proc Natl Acad Sci USA 94, 13661–13665.

Petersen OW, Rønnov-Jessen L, Howlett AR, Bissell MJ (1992). Interaction with basement membrane serves to rapidly distinguish growth and differentiation pattern of normal and malignant human breast epithelial cells. Proc Natl Acad Sci USA 89, 9064–9068.

Przybyla L, Lakins JN, Sunyer R, Trepat X, Weaver VM (2016). Monitoring developmental force distributions in reconstituted embryonic epithelia. Methods 94, 101–113.

Rigort A, Plitzko JM (2015). Cryo-focused-ion-beam applications in structural biology. Arch Biochem Biophys 581, 122–130.

Ross TD, Coon BG, Yun S, Baeyens N, Tanaka K, Ouyang M, Schwartz MA (2013). Integrins in mechanotransduction. Curr Opin Cell Biol 25, 613–618.

Rubashkin MG, Cassereau L, Bainer R, DuFort CC, Yui Y, Ou G, Paszek MJ, Davidson MW, Chen YY, Weaver VM (2014). Force engages vinculin and

promotes tumor progression by enhancing PI3K activation of phosphatidylinositol (3,4,5)-triphosphate. Cancer Res 74, 4597–4611.
Santner SJ, Dawson PJ, Tait L, Soule HD, Eliason J, Mohamed AN, Wolman SR, Heppner GH, Miller FR (2001). Malignant MCF10CA1 cell lines derived from premalignant human breast epithelial MCF10AT cells. Breast Cancer Res Treat 65, 101–110.
Sartori A, Gatz R, Beck F, Rigort A, Baumeister W, Plitzko JM (2007). Correlative microscopy: bridging the gap between fluorescence light microscopy and cryo-electron tomography. J Struct Biol 160, 135–145.
Schaffer M, Pfeffer S, Mahamid J, Kleindiek S, Laugks T, Albert S, Engel BD, Rummel A, Smith AJ, Baumeister W, *et al.* (2019). A cryo-FIB lift-out technique enables molecular-resolution cryo-ET within native *Caenorhabditis elegans* tissue. Nat Methods 16, 757–762.
Schwartz CL, Sarbash VI, Ataullakhanov FI, McIntosh JR, Nicastro D (2007). Cryo-fluorescence microscopy facilitates correlations between light and cryo-electron microscopy and reduces the rate of photobleaching. J Microsc 227, 98–109.
Schwartz MA (2010). Integrins and extracellular matrix in mechanotransduction. Cold Spring Harb Perspect Biol 2, a005066.
Sen S, Engler AJ, Discher DE (2009). Matrix strains induced by cells: computing how far cells can feel. Cell Mol Bioeng 2, 39–48.
Shinsato Y, Doyle AD, Li W, Yamada KM (2020). Direct comparison of five different 3D extracellular matrix model systems for characterization of cancer cell migration. Cancer Rep (Hoboken) 3, e1257.
Soule HD, Maloney TM, Wolman SR, Peterson WD, Brenz R, McGrath CM, Russo J, Pauley RJ, Jones RF, Brooks SC (1990). Isolation and characterization of a spontaneously immortalized human breast epithelial cell line, MCF-10. Cancer Res 50, 6075–6086.
Streuli CH, Bailey N, Bissell MJ (1991). Control of mammary epithelial differentiation: basement membrane induces tissue-specific gene expression in the absence of cell-cell interaction and morphological polarity. J Cell Biol 115, 1383–1395.
Sun Z, Guo SS, Fässler R (2016). Integrin-mediated mechanotransduction. J Cell Biol 215, 445–456.
Toro-Nahuelpan M, Zagoriy I, Senger F, Blanchoin L, Théry M, Mahamid J (2020). Tailoring cryo-electron microscopy grids by photo-micropatterning for in-cell structural studies. Nat Methods 17, 50–54.
Tse JR, Engler AJ (2010). Preparation of hydrogel substrates with tunable mechanical properties. Curr Protoc Cell Biol Chapter 10, Unit 10.16.
Turk M, Baumeister W (2020). The promise and the challenges of cryo-electron tomography. FEBS Lett 594, 3243–3261.
Volkmann N, Hanein D (1999). Quantitative fitting of atomic models into observed densities derived by electron microscopy. J Struct Biol 125, 176–184.
Wang YL, Pelham RJ (1998). Preparation of a flexible, porous polyacrylamide substrate for mechanical studies of cultured cells. Methods Enzymol 298, 489–496.